Research Article

Journal of Environmental Nanotechnology

Green Synthesis of MgO Nanoparticles Using *Aerva lanata* Leaf Extract: Physicochemical Characterization, Antibacterial Activity and Cytotoxicity

Dhananjay Bhaurao Awachat[1], P. Satishkumar[2], Anju Rani[3], A. Athisaya Sagaya Rajan[4], Omehswar D. Verma[5] and K. Raajananthini[6]*

[1]Department of Civil Engineering, K D K College of Engineering, Nagpur, MH, India
[2]Department of Mechanical Engineering, Rathinam Technical Campus, Coimbatore, TN, India
[3]Department of Physics, School of Engineering and Technology, CGC University, Mohali, PB, India
[4]Department of Mechanical Engineering, Nehru Institute of Engineering and Technology, Coimbatore, TN, India
[5]Department of Applied Physics, Yeshwantrao Chavan College of Engineering, Nagpur, MH, India
[6]Department of Science and Humanities, Rathinam Technical Campus, Coimbatore, TN, India
Received: 01.08.2026 Accepted: 31.08.2026 Published: 30.09.2026
*raajananthinik@gmail.com

ABSTRACT

The increasing complexity of contemporary health disorders has created a need for alternative therapeutic strategies. Plant-mediated nanomaterials offer promising biomedical applications because of their distinctive physicochemical and biological characteristics. This investigation employed *Aerva lanata* leaf extract as a natural complexing and stabilizing medium for the eco-friendly preparation of magnesium oxide (MgO NPs) and assessed antibacterial and anticancer activities. The synthesized MgO nanoparticles were characterized using UV–visible spectroscopy, X-ray diffraction, Fourier-transform infrared spectroscopy, dynamic light scattering and zeta-potential analysis. XRD confirmed cubic periclase MgO with an average crystallite size of 24.68 nm. The nanoparticles exhibited antibacterial activity against *Escherichia coli* and *Klebsiella pneumoniae*, with greater activity against *E. coli* (MIC: 125.36 ± 12.48 µg/mL; inhibition zone: 20.46 ± 1.18 mm). They also produced concentration-dependent cytotoxicity against PC-3 prostate cancer cells, with an IC_{50} of approximately 87.43 µg/mL. These outcomes demonstrate that *A. lanata*-assisted MgO NPs may serve as environmentally sustainable materials with potential antibacterial and anticancer applications.

Keywords: Sustainability; Anticancer activity; Disk-diffusion; Cytotoxicity; UV-absorption.

1. INTRODUCTION

The growing demand for sustainable, lightweight, and biologically compatible materials has encouraged the replacement of energy-intensive synthesis routes and synthetic reinforcements with green nanotechnology and natural-material-based systems (Krishnasamy *et al.* 2025). Machine-learning-guided material design has further reduced experimental trials while facilitating the identification of low-cytotoxic nanomaterials with strong antioxidant activity and cellular compatibility (Ebenezer *et al.* 2026). Statistical modelling and multi-objective optimization have also enabled the development of lightweight composites with improved mechanical and thermal performance for automotive, aerospace, structural, and industrial applications (Krishnasamy *et al.* 2026). Moreover, synthesis conditions strongly influence nanoparticle crystallinity and functionality; hydrothermally synthesized nanoparticles have demonstrated enhanced photocatalytic and antibacterial performance when incorporated into superhydrophobic antimicrobial textile coatings (Ganvir *et al.* 2026b).

Plant-mediated synthesis represents an environmentally sustainable approach in which phytochemicals act as reducing, stabilizing, and capping agents during nanoparticle formation. *Aerva lanata* is particularly attractive because of its diverse phytochemical constituents and established biological properties. Silver nanoparticles synthesized using its flower extract exhibited an average size of approximately 7 nm and demonstrated antibacterial, antioxidant, and sunlight-driven photocatalytic activities (Palithya *et al.* 2022). Similarly, *A. lanata*-mediated ZnO nanoparticles produced inhibition zones of 11–18 mm against different bacterial strains at 100 µg/mL (Ganesan *et al.* 2023). Green-synthesized nickel nanoparticles using *Aerva lanata* extract with sizes up to 40 nm achieved 100% fungal inhibition and 85% bacterial inhibition (Jayamani *et al.* 2025), while 45.05 nm AgNPs exhibited significant free-radical scavenging, strong antibacterial, and moderate antifungal activities (Ganesan *et al.* 2024). Furthermore, the antioxidant, xanthine oxidase-inhibitory, and anti-urolithiatic activities of *A. lanata* and *Aerva javanica* extracts demonstrate their wider therapeutic potential (Sanjai *et al.* 2025; Sanjana *et al.* 2025).

Among metal oxides, MgO has attracted considerable interest because of its physicochemical stability, tunable surface characteristics, biocompatibility, antimicrobial behaviour, and environmental remediation capacity. MgO nanoparticles synthesized using *Ficus carica* leaf extract displayed precursor-dependent crystallite size, optical band gap, and surface roughness, with magnesium-nitrate-derived MgO showing properties favourable for antibacterial applications (Obead and Abbas, 2025). *Chrysanthemum indicum*-mediated MgO nanoparticles, with an average size of 20.5 nm, exhibited concentration-dependent antioxidant activity and good biocompatibility (Periakaruppan *et al*. 2025). Likewise, *Hevea brasiliensis*-derived MgO nanoparticles achieved 87.78% methylene blue degradation, 93.33% mineralization, and strong antibacterial activity against *E. coli* and *S. aureus* (Otabor and Ikhuoria, 2026). Orange-peel-mediated MgO nanoparticles also maintained more than 80% cell viability and demonstrated moderate antimicrobial and antibiofilm activity, while providing greater insight into the role of phytochemicals in controlling nanoparticle formation (Radulescu *et al.* 2025). Sanjana *et al*. (2025) similarly reported antimicrobial and cytotoxic responses for plant-mediated calcium oxide nanoparticles, supporting the relevance of green metal-oxide nanomaterials for biological applications.

The incorporation of MgO into multicomponent systems can generate synergistic structural, optical, catalytic, and biological effects. CuO@MgO core–shell nanoparticles exhibited antibacterial activity against Bacillus cereus and Proteus mirabilis, while molecular docking indicated favourable interactions with bacterial proteins (Najm *et al.* 2026). MgO–NiO nanocomposites calcined at 450 °C showed superior antibacterial and antioxidant activities, and both the 450 and 550 °C samples produced less than 2% hemolysis (Gajendiran *et al.* 2025). Green-synthesized Mg/ZnO nanocomposites achieved 99.42% tetracycline and 95.35% crystal violet degradation within 90 min, together with enhanced antibacterial activity (Rana *et al.* 2025). Similarly, Cu/Zn-doped MgO nanoparticles attained 92% Rhodamine B and 99% methyl orange degradation because doping reduced the band gap and improved photocatalytic performance (Thakur *et al*. 2025).

MgO-based hybrid nanomaterials have also demonstrated promising biomedical performance. A *Tinospora cordifolia*-mediated CuO–MgO core–shell nanocomposite exhibited strong antioxidant activity and only 0.57% hemolysis at 100 µg/mL (Vamsi *et al*. 2025). Mycosynthesized MnO–MgO nanoparticles displayed broad-spectrum antibacterial, bactericidal, antibiofilm, antibiotic-synergistic, and selective anticancer effects (Elkady *et al.* 2026). ZnO/MgO nanoparticles synthesized using *Echium amoenum* flower extract achieved a production yield of 95.4% and inhibited MCF-7 cancer cells with an IC_{50} of 94.40 µg/mL (Ghasemzadeh *et al.* 2025). Ag-doped MgO–ZnO nanocomposites prepared using *Cassia alata* extract also demonstrated antimicrobial activity and dose-dependent cytotoxicity against A549 lung cancer cells, with an IC_{50} of 45.8 µg/mL (Kattookaran *et al*. 2025).

The versatility of MgO-containing systems extends to bioceramics, radiation shielding, and wastewater treatment. Merwinite-dominant CaO–MgO–SiO_2 bioceramics exhibited controlled degradation, suitable biocompatibility, and Vickers hardness values of 376.7–399.7 HV, supporting their potential for bone regeneration and implant applications (Imtiaz *et al.* 2025). MgO-containing apatite–wollastonite glass ceramics with 2–8 wt% Y_2O_3 were fabricated using a powder-metallurgy process. The developed materials demonstrated promising potential for biomedical applications (Al-Buriahi *et al.* 2025). $BaAl_2O_4$/MgO/$BaCO_3$ nanocomposites calcined at 500 °C achieved a crystal violet adsorption capacity of 377.36 mg/g, followed Langmuir equilibrium and pseudo-first-order kinetic models and maintained good regeneration performance (Al-Wasidi and Abdelrahman, 2026). Green-synthesized CaO, MgO, ZnO, and TiO_2 nanoparticles derived from Brassica oleracea also demonstrated improved colloidal stability, minimal hemolysis, and preservation of red-blood-cell morphology (Gamal *et al.* 2026).

Although *Aerva lanata* has been used to synthesize Ag, ZnO, and Ni nanoparticles, its application in the plant-mediated synthesis of MgO nanoparticles remains insufficiently investigated. In particular, limited information is available on the combined antibacterial and anticancer performance of *A. lanata*-mediated MgO nanoparticles. Therefore, the novelty of this study lies in using *A. lanata* leaf extract as a natural complexing and stabilizing medium to produce MgO nanoparticles and systematically evaluating their antibacterial activity against *E. coli* and *K. pneumoniae* and cytotoxicity against PC-3 prostate cancer cells.

2. MATERIALS AND METHODOLOGY

2.1 Plant Material Collection

Fresh *Aerva lanata* leaves were collected from naturally growing plants, and healthy, undamaged leaves were selected and transported to the laboratory in clean containers.

2.2 Preparation of Plant Extract

Fresh *Aerva lanata* leaves were thoroughly rinsed 3 times with distilled water to eliminate adhering dust and surface contaminants. Cleaned leaves were shade-dried to a constant mass and ground into fine powder. Subsequently, 20 g of leaf powder was dispersed

in 200 mL of Distilled water and heated at 70 °C with continuous magnetic stirring at 200 rpm for 45 min. After cooling to ambient temperature, the mixture was filtered through filter paper. The resulting aqueous extract was transferred into an airtight amber-glass container and stored at 4 °C until it was used for the green preparation of MgO nanoparticles.

2.3 Green Synthesis of MgO Nanoparticles

Aerva lanata is a medicinal herb containing phytochemicals such as phenolics, flavonoids, tannins, alkaloids and polysaccharides, which can assist nanoparticle formation and stabilization. For MgO preparation, a 0.1 M [$Mg(NO_3)_2 \cdot 6H_2O$] solution was prepared in deionized water. The aqueous leaf extract and precursor solution were blended at a 1:4 volume ratio and continuously stirred at 60 °C for 60 min. Th pH was gradually adjusted to 10 with 1 M NaOH to promote magnesium hydroxide precipitation. The precipitate was separated by centrifugation at 10,000 rpm for 15 min and washed three times, alternately using deionized water and ethanol, to remove residual ions and phytochemicals. The recovered precipitate was dried at 80 °C for 12 h and heated to 450 °C at a rate of 5 °C min^{-1}. It was calcined. at 450 °C for 2 h and subsequently cooled naturally to room temperature(Ganvir *et al.* 2026a) .

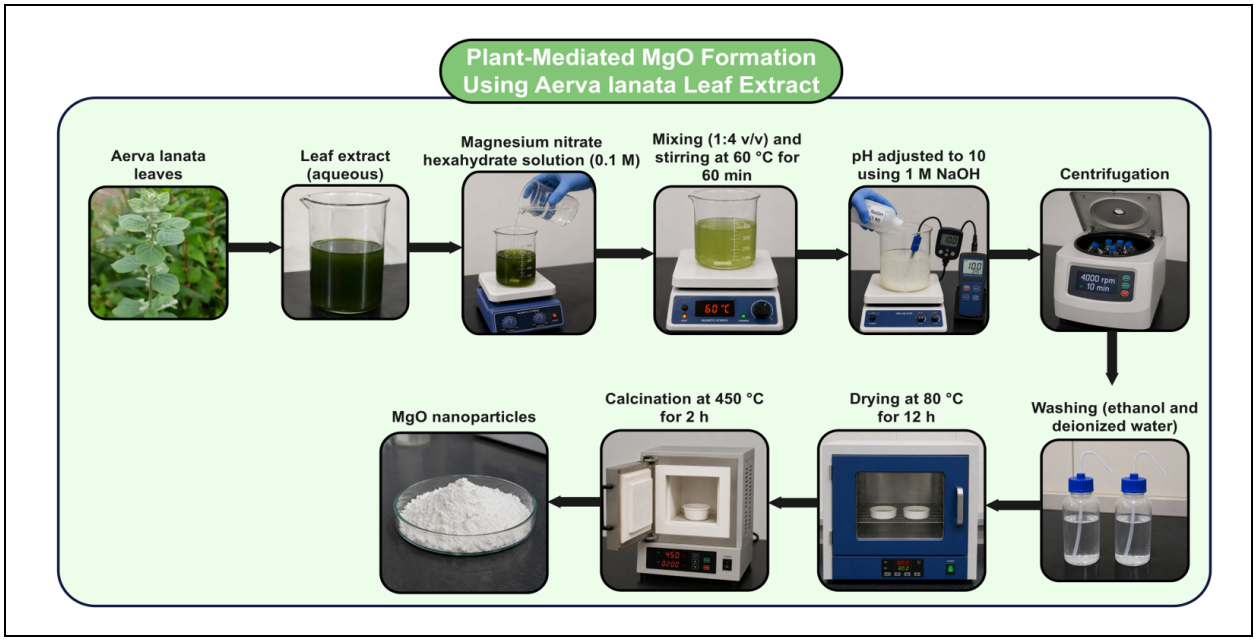

Fig. 1: Formation of plant-mediated MgO formation

2.4 Characterization of MgO NPs

Optical characteristics of prepared MgO NPs were investigated by a Shimadzu UV-2600 UV–visible spectrophotometer over 200–800 nm at a spectral interval of 1 nm. Measurements were conducted at 25 ± 2 °C in a quartz cell with a 1 cm optical path, with deionized water serving as the blank. Spectra collected at different storage periods were compared to assess optical stability; minimal displacement of the principal absorption band indicated satisfactory stability.

For FTIR examination, the washed MgO precipitate was dried at 80 °C for 12 h and calcined at 450 °C for 2 h. Approximately 1 mg of powdered material was blended with 100 mg of spectroscopic-grade KBr and compressed into a pellet. Spectra were acquired using a Bruker ALPHA II FTIR spectrometer between 4000 and 400 cm^{-1} at 4 cm^{-1}. This analysis identified residual plant-derived functional groups and characteristic Mg–O vibrations.

Crystalline phase and crystallite size were evaluated with a PANalytical X'Pert PRO diffractometer using Cu Kα radiation across 2θ. Hydrodynamic diameter, polydispersity index and surface charge were determined by Malvern Zetasizer Nano ZS at 25 °C.

2.5 Phytochemical Functional-group Analysis

FTIR spectroscopy was employed to identify major functional groups in *Aerva lanata* extract. The recorded bands indicated phytochemicals potentially involved in magnesium-ion complexation, MgO nucleation and nanoparticle stabilization.

2.6 Biological Activities of Biogenic MgO Nanoparticles

2.6.1 Disk-diffusion Assay

Fresh suspensions of *Escherichia coli* and *Klebsiella pneumoniae* were adjusted to 0.5 McFarland turbidity and uniformly spread over Mueller–Hinton agar

using sterile swabs. Sterile paper disks loaded with 20 µL of *Aerva lanata*-mediated MgO nanoparticle suspension were positioned on each plate. Amikacin and ciprofloxacin disks served as positive controls for *E. coli* and *K. pneumoniae*, respectively, while solvent-loaded disks served as negative controls. Disk-diffusion assays were conducted using three independent biological replicates (n = 3). Following incubation at 36 °C for 1 day, inhibition-zone diameters were measured in millimetres.

2.6.2 MIC Analysis

The MIC was measured using broth microdilution procedure. Mueller–Hinton broth (100 µL) was dispensed into a 96-well plate, and MgO nanoparticle concentrations from 15.625 to 1000 µg/mL was prepared by twofold serial dilution. Bacterial inoculum was added to obtain final density of 5×10^5 CFU/mL. Antibiotic, untreated-growth and broth-only wells represented positive, growth and sterility controls, respectively. After incubation at 35 ± 2 °C for 1 day, low concentration with no visible turbidity were recorded MIC.

2.6.3 Minimum Bactericidal Concentration

Aliquots from clear wells at and above the MIC were spread on nutrient agar plates and incubated at 35 ± 2 °C for 1 day. MgO nanoparticles producing no visible colonies, corresponding to at least 99.9% bacterial reduction, were identified as the MBC.

2.6.4 Time Kill Kinetics

Bacterial cultures containing approximately 1×10^6 CFU/mL were treated with MgO nanoparticles at their respective MBC values. Samples collected at 0, 2, 4, 6, 12 and 24 h were serially diluted and plated at tryptic soy agar. Colonies were counted after 24 h of incubation, and viable populations were expressed as $\log_{10}$ CFU/mL. Untreated cultures served as growth controls. A reduction of at least 3 $\log_{10}$ CFU/mL relative to the initial inoculum indicated bactericidal activity.

2.6.5 *In Vitro* Cytotoxicity of Green MgO Nanoparticles in PC-3 Cells

PC-3 cells were seeded into 96-well plates at 5×10^3 cells/well and incubated for 24 h. Cells were subsequently exposed to MgO nanoparticles at 0.02–200 µg/mL for 48 h. MTT were given to concentration of 0.5 mg/mL, incubation at 36°C for 3 h. After removing the medium, crystals were dissolved in 200 µL of DMSO.

2.6.6 Statistical Analysis

All biological experiments were performed using three independent biological replicates (n = 3), and the results are expressed as mean ± standard deviation. Statistical differences among groups were evaluated using one-way analysis of variance followed by Tukey's multiple comparison post-hoc test in GraphPad Prism. Differences were considered statistically significant at $p < 0.05$.

3. RESULTS AND DISCUSSION

3.1 Characterization of Green-synthesized MgO Nanoparticles

The formation, optical behaviour and crystalline characteristics of *Aerva lanata*-mediated MgO nanoparticles was evaluated by UV–Vis spectroscopy and XRD.

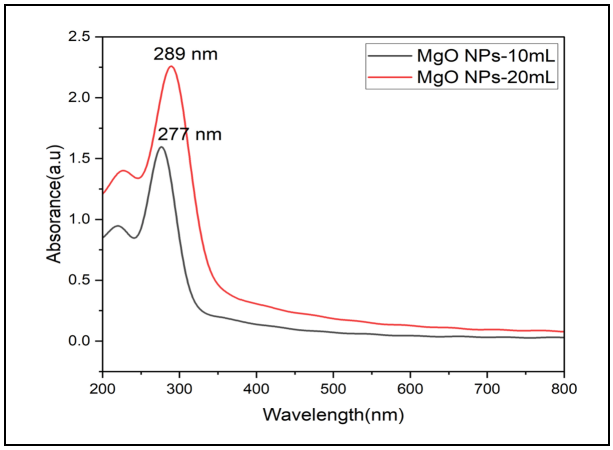

Fig. 2: UV–Vis spectrum of MgO

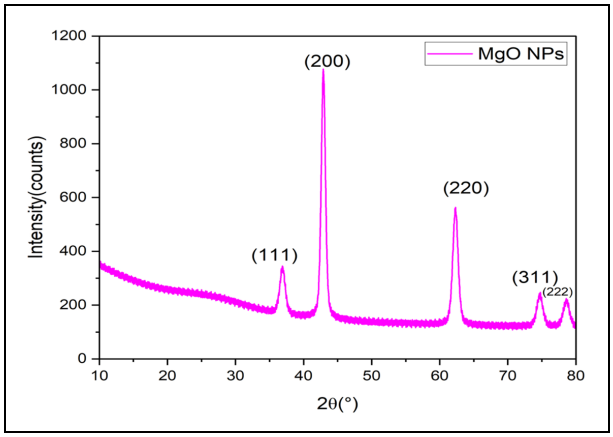

Fig. 3: XRD pattern of MgO

UV–Vis spectrum displayed a prominent absorption band at 277 nm and 289 nm, supporting successful formation of MgO nanoparticles (Fig. 2). This ultraviolet absorption originates mainly from electronic transitions across the MgO band structure and defect-related energy states rather than surface plasmon resonance. The absence of substantial absorption in the visible region further indicated the characteristic wide-band-gap behaviour. According to previous research,

UV–Vis analysis of *Aerva lanata* leaf-mediated ZnO nanorods revealed the characteristic absorption band associated with ZnO formation. The estimated optical band-gap energy was 3.24 eV, confirming their semiconductor behaviour (Suresh *et al.* 2022).

The XRD pattern presented in Fig. 3 showed distinct peaks at 2θ of 37.0°, 43.0°, 62.3°, 74.5° and 78.2°. These reflections were assigned to the (111), (200), (220), (311) and (222) planes, with a cubic periclase structure of MgO. The most intense reflection was detected at 43.0°, corresponding to the (200) plane. The observed diffraction peaks were consistent with the standard cubic periclase MgO pattern (JCPDS/PDF Card No. 45-0946), confirming the formation of phase-pure crystalline MgO. The absence of prominent additional reflections suggested satisfactory phase purity after calcination. Crystallite size was estimated from the full width at half maximum of the principal diffraction peaks by the Debye–Scherrer equation. The average size was 24.68 nm, demonstrating the nanocrystalline nature of the prepared MgO material. In previous studies, XRD analysis of *Aerva lanata* flower-mediated silver nanoparticles confirmed their crystalline nature and successful phase formation. The characteristic diffraction peaks verified the formation of metallic AgNPs without significant impurity phases (Raguvaran *et al.* 2025).

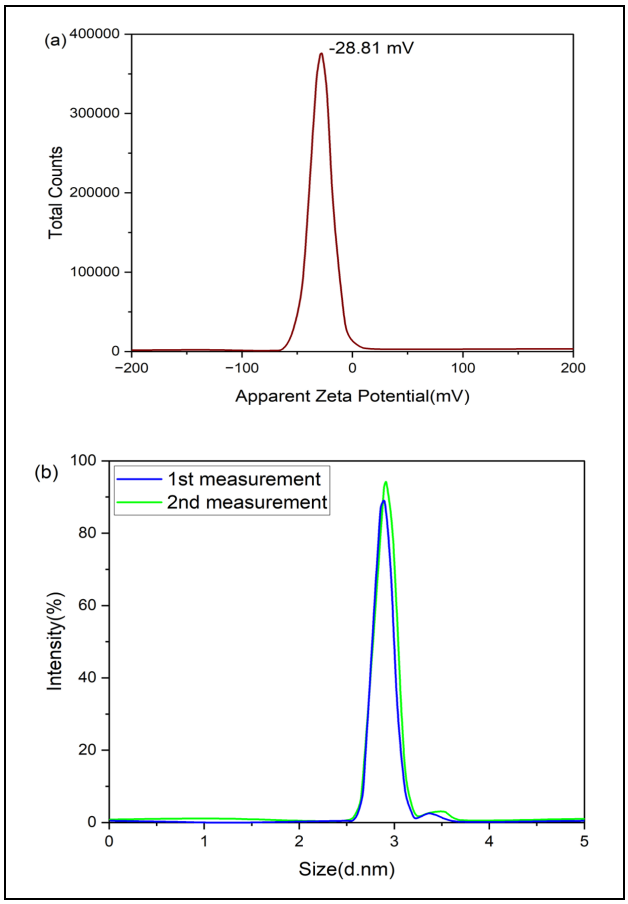

Fig. 4: DLS properties of MgO nanoparticles

The colloidal characteristics of *Aerva lanata*-mediated MgO nanoparticles were determined through zeta-potential and DLS measurements (Fig. 4). The nanoparticles exhibited an average zeta potential of −28.81 mV, indicating moderate electrostatic stability (Fig. 4a). DLS analysis showed a principal peak at approximately $\log_{10}(d/nm) = 2.9$, corresponding to a hydrodynamic diameter of approximately 794 nm (Fig. 4b). The crystallite size determined by XRD (24.68 nm) represents the average size of individual crystalline domains, whereas the DLS value (~794 nm) represents the hydrodynamic diameter of particles and aggregates dispersed in the liquid medium. The substantially larger DLS diameter indicates considerable nanoparticle aggregation, which may arise from interparticle attraction, insufficient dispersion and the hydrated phytochemical layer present on the MgO surface. Therefore, the DLS value should not be interpreted as the size of an individual MgO crystallite.

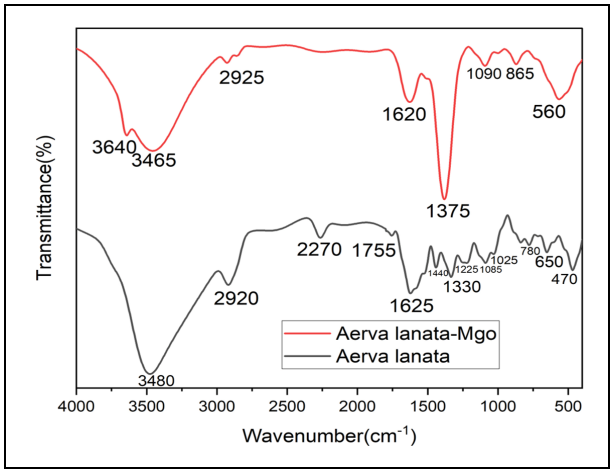

Fig. 5: FTIR spectra of biogenic MgO

FTIR spectroscopy was used to compare functional groups of *Aerva lanata* extract and the plant-mediated MgO NPs. The extract displayed major absorption bands at approximately 3480, 2920, 2270, 1755, 1625, 1440, 1330, 1225, 1085, 1025, 780, 650 and 470 cm^{-1}. These bands were associated with aliphatic C–H, O–H, C–O and aromatic C=C -containing phytochemicals. After MgO formation, shifted or reduced bands appeared at approximately 3640, 3465, 2925, 1620, 1375, 1090 and 865 cm^{-1}. A strong absorption region below 560 cm^{-1} was assigned to Mg–O lattice vibrations (Fig. 5). Changes in the phytochemical bands suggested their participation in magnesium-ion complexation, particle nucleation and surface stabilization. The Mg–O vibrations confirmed successful MgO NPs (Table 1). As reported in previous studies, FTIR analysis of pure ZnO, *Aerva lanata*-ZnO, *Millettia pinnata*-ZnO, and their Cu-doped nanoparticles identified the associated functional groups and chemical interactions. The characteristic absorption bands confirmed Zn–O bonding and interactions between plant-

derived phytochemicals and the Cu-doped ZnO structure (Renuka *et al.* 2023).

Table 1. Antibacterial inhibition-zone diameters

Organism	Negative Control (mm)	MgO NPs (mm)	Antibiotic (mm)
E. coli	0.00	20.46 ± 1.18	23.28 ± 1.34
K. pneumoniae	0.00	15.38 ± 1.07	27.16 ± 1.42

Values are expressed as mean ± standard deviation of three independent biological replicates (n = 3). Antibiotic-treated samples served as positive controls, while solvent-treated samples served as negative controls.

Table 2. MIC and MBC results

Organism	Antibiotic MIC (µg/mL)	MgO NPs MBC (µg/mL)	MgO NPs MIC (µg/mL)	Antibiotic MBC (µg/mL)
E. coli	4.00 ± 0.50	250.72 ± 20.36	125.36 ± 12.48	8.00 ± 1.00
K. pneumoniae	0.50 ± 0.06	500.64 ± 36.28	250.48 ± 21.35	1.00 ± 0.13

MIC and MBC values are expressed as mean ± standard deviation of three independent biological replicates (n = 3). Statistical comparisons were conducted using one-way ANOVA followed by Tukey's multiple-comparison test, with $p < 0.05$ considered statistically significant. The MgO nanoparticle MIC and MBC values were lower for *E. coli* than for *K. pneumoniae*, indicating greater susceptibility of *E. coli*. The MBC/MIC ratio was approximately 2 for both organisms, confirming bactericidal activity.

3.2 Disk Diffusion

The mean inhibition-zone diameters produced by *Aerva lanata*-mediated MgO nanoparticles against *E. coli* and *K. pneumoniae* were 20.46 ± 1.18 and 15.38 ± 1.07 mm, respectively. No inhibition was observed for the negative control. Amikacin produced a 23.28 ± 1.34 mm zone against *E. coli*, whereas ciprofloxacin generated a 27.16 ± 1.42 mm zone against *K. pneumoniae*. The results indicated that MgO nanoparticles were more effective against *E. coli* than *K. pneumoniae*.

3.3 MIC Results

MIC of MgO nanoparticles was 250.48 ± 21.35 µg/mL for *K. pneumoniae* and 125.36 ± 12.48 µg/mL for *E. coli*. The corresponding antibiotic MIC values were 0.50 ± 0.06 µg/mL for ciprofloxacin and 4.00 ± 0.50 µg/mL for amikacin. Therefore, the lower nanoparticle concentration required against *E. coli* demonstrated its greater susceptibility compared with *K. pneumoniae*.

3.4 MBC Results

MgO nanoparticles produced MBC values of 250.72 ± 20.36 and 500.64 ± 36.28 µg/mL against *E. coli* and *K. pneumoniae*, respectively. The antibiotic MBC values were 8.00 ± 1.00 and 1.00 ± 0.13 µg/mL, respectively. The MBC results confirmed concentration-dependent bactericidal activity, with *E. coli* displaying greater sensitivity to the prepared MgO nanoparticles. In prior studies, a low MIC of 0.25 mg/mL demonstrated strong inhibitory activity against all tested Gram-negative bacterial strains. MBC/MIC ratios ≤ 4 confirmed potent bactericidal activity, comparable to or exceeding standard antibiotics (Fonye *et al.* 2026).

3.5 Time Kill Kinetics

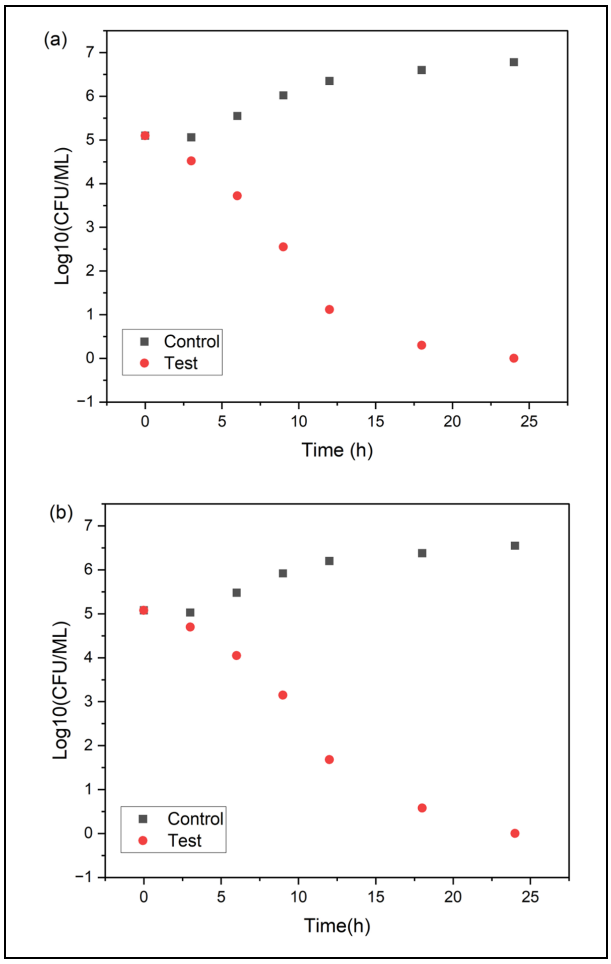

Fig. 6: Bacterial inactivation: (a) *E. coli*, and (b) *K. pneumoniae*

Fig. 6(a) and (b) illustrate the time-dependent antibacterial action of *Aerva lanata*-mediated MgO nanoparticles against *K. pneumoniae* and *E. coli* over 24 h. In both test groups, the viable bacterial population decreased from approximately 5.1 $\log_{10}$ CFU/mL at 0 h to 0 $\log_{10}$ CFU/mL at 24 h, corresponding to an approximately 5.1-log reduction. The untreated control

populations increased progressively during the same period. Both test groups exceeded the 3-log reduction threshold commonly used to indicate bactericidal activity. However, *E. coli* showed a faster decline than *K. pneumoniae*, particularly during the intermediate exposure periods. Previous studies have demonstrated that strong antibacterial activity was observed against *B. subtilis, E. coli, K. pneumoniae,* and *S. aureus*. Dose-dependent biofilm disruption and bacterial death occurred through ROS generation and membrane damage (Nagaraj *et al.* 2025).

3.6 Cytotoxicity Assay

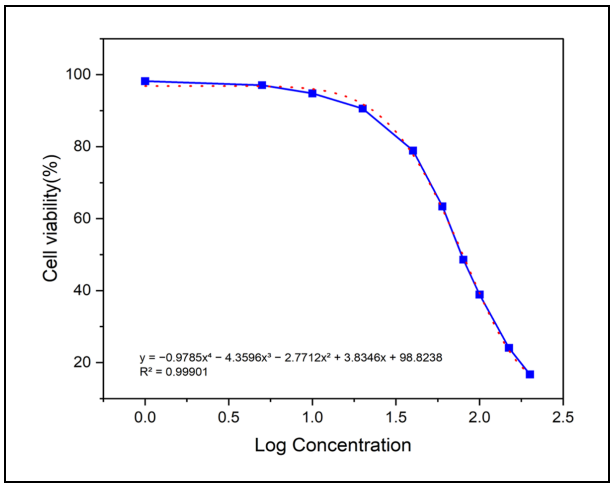

Fig. 7: Dose–response of MgO nanoparticles

The cytotoxic effect of *Aerva lanata*-mediated MgO nanoparticles against PC-3 prostate cancer cells was evaluated using the MTT assay. Cells were exposed to MgO nanoparticle concentrations ranging from 0.02 to 200 µg/mL for 48 h. As shown in Fig. 7, cell viability decreased progressively with increasing nanoparticle concentration. Nonlinear dose–response analysis produced an estimated IC_{50} value of 87.43 µg/mL ($\log_{10}$ concentration = 1.942), with an R^2 value of 0.99901. These results demonstrate concentration-dependent cytotoxicity against PC-3 cells. However, because a non-cancerous normal-cell control was not included, the selectivity and therapeutic safety of the MgO nanoparticles cannot be established. Therefore, the reported IC_{50} should not be interpreted as evidence of selective anticancer activity. Future studies should evaluate cytotoxicity against normal prostate cells and calculate the selectivity index (Dash *et al.* 2025).

Plant-mediated preparation of metal-oxide nanoparticles provides a comparatively sustainable approach that reduces dependence on hazardous organic reagents. In the present investigation, *Aerva lanata* leaf extract facilitated the formation of MgO nanoparticles through the complexation of Mg^{2+} ions, formation of a $Mg(OH)_2$ intermediate and subsequent thermal conversion into crystalline MgO. Phenolics, flavonoids, tannins, alkaloids and polysaccharides in the extract may regulate nucleation, restrict excessive particle growth and stabilize the nanoparticle surface.

UV–Vis spectrum shows distinct absorption bands near 277 and 289 nm, confirming the characteristic optical response of MgO nanoparticles. Unlike metallic nanostructures, this ultraviolet band is attributed mainly to electronic transitions across the MgO band structure and defect-associated energy states. The limited absorption observed at visible region was consistent with wide-band-gap nature of MgO.

FTIR analysis provided evidence for the participation of plant metabolites during nanoparticle formation. The leaf extract displayed bands near 3480, 2920, 2270, 1755, 1625, 1440, 1330, 1225, 1085, 1025, 780, 650 and 470 cm^{-1}. These signals were assigned to aliphatic O–H, C–O and aromatic C=C. Following MgO formation, changes were observed at approximately 3640, 3465, 2925, 1620, 1375, 1090 and 865 cm^{-1}, indicating interactions between phytochemical functional groups and the nanoparticle surface. The prominent bands near 560 cm^{-1} were assigned to Mg–O lattice vibrations and verified oxide formation. Therefore, the extract primarily functioned as a complexing, growth-controlling and stabilizing medium.

The XRD pattern contained characteristic reflections at 37.0°, 43.0°, 62.3°, 74.5° and 78.2°, corresponding to (111), (200), (220), (311) and (222) of cubic periclase MgO. The strongest reflection at 43.0° represented the (200) plane. No prominent secondary-phase peaks were detected, suggesting satisfactory phase purity following calcination at 450 °C. Peak broadening confirmed the nanocrystalline character of the product, while the Debye–Scherrer calculation yielded an average crystallite size of approximately 24.68 nm.

DLS analysis gave a mean hydrodynamic diameter of approximately 794 nm, corresponding to a principal peak at $\log_{10}(d/nm) \approx 2.9$. The average zeta potential of −28.81 mV indicated moderate colloidal stability, probably supported by negatively charged phytochemical residues retained on the MgO surface.

The prepared MgO nanoparticles showed concentration-dependent antibacterial activity against *K. pneumoniae* and *E. coli*. Inhibition-zone diameters of 20.46 ± 1.18 and 15.38 ± 1.07 mm were recorded, respectively. The corresponding MIC values were 125.36 ± 12.48 and 250.48 ± 21.35 µg/mL, while MBC values reached 250.72 ± 20.36 and 500.64 ± 36.28 µg/mL. These results indicate that *E. coli* was more susceptible to the MgO formulation.

Time–kill analysis supported the bactericidal behaviour of the nanoparticles. Over 24 h, the viable populations of both *E. coli* and *K. pneumoniae* decreased

from approximately 5.1 to 0 $\log_{10}$ CFU/mL, representing an approximately 5.1-log reduction. Both values exceeded the 3-log criterion for bactericidal activity, although bacterial elimination occurred more rapidly against *E. coli*.

MgO nanoparticles may damage bacterial cells through several complementary processes. Their interaction with the cell envelope can disturb membrane integrity and increase permeability. Surface defects may promote reactive oxygen species formation, while partial Mg^{2+} release and localized alkalinity can disrupt cellular homeostasis. Oxidative stress can subsequently damage membrane lipids, proteins and genetic material, leading to reduced metabolic activity and cell death. Differences in capsule structure, membrane composition and defensive systems may explain the lower susceptibility of *K. pneumoniae*.

The MTT results demonstrated a concentration-dependent reduction in PC-3 cell metabolic activity, with an IC_{50} of 87.43 µg/mL after 48 h. The observed response may be associated with oxidative stress, membrane disruption or mitochondrial impairment, as suggested for MgO nanoparticles in previous studies. However, ROS generation, mitochondrial dysfunction and apoptosis were not experimentally evaluated in the present investigation. Therefore, no specific mechanism of cell death can be confirmed from the MTT results alone. Further studies involving intracellular ROS measurements, mitochondrial membrane potential analysis, apoptosis markers and cell morphology assessment are required to establish the underlying cytotoxic mechanism.

Overall, *Aerva lanata*-mediated MgO nanoparticles exhibited defined crystalline, morphological and colloidal properties together with measurable antibacterial and cytotoxic activities. Their biological performance may be influenced by nanoscale dimensions, surface defects and retained plant-derived compounds. Future investigations should include normal-cell controls, selectivity-index calculations, mechanistic assays and in vivo safety studies before therapeutic suitability can be established.

4. CONCLUSION

This study demonstrated the plant-mediated synthesis of MgO nanoparticles using *Aerva lanata* leaf extract as a natural complexing and stabilizing medium. UV–visible absorption bands at 277 and 289 nm supported nanoparticle formation, while XRD confirmed cubic periclase MgO with an average crystallite size of 24.68 nm. The nanoparticles exhibited antibacterial activity against *Escherichia coli* and *Klebsiella pneumoniae*, with greater activity against *E. coli*, which showed an MIC of 125.36 ± 12.48 µg/mL and an inhibition-zone diameter of 20.46 ± 1.18 mm. The nanoparticles also produced concentration-dependent cytotoxicity against PC-3 prostate cancer cells, with an IC_{50} of approximately 87.43 µg/mL after 48 h. However, because normal-cell controls were not included, these findings do not establish selective anticancer activity or therapeutic safety. Further investigations involving normal-cell cytotoxicity, selectivity-index calculation, ROS and apoptosis assays, long-term biocompatibility studies, and in vivo validation are required before biomedical or therapeutic applications can be considered.

FUNDING

This research received no specific grant from any funding agency in the public, commercial, or not-for-profit sectors.

CONFLICTS OF INTEREST

The authors declare that there is no conflict of interest.

COPYRIGHT

This article is an open-access article distributed under the terms and conditions of the Creative Commons Attribution (CC BY) license (http://creativecommons.org/licenses/by/4.0/).

REFERENCES

Al-Buriahi, M. S., Alzahrani, J. S., Iliyasu, U., Alomayrah, N. and İbrahimoğlu, E., Fabrication, structural, and mechanical characterization of Y_2O_3-reinforced Apatite-Wollastonite glass-ceramics for biomedical and radiation shielding applications, *J. Alloys Compds.*, 1042, 184201 (2025). https://doi.org/10.1016/j.jallcom.2025.184201

Al-Wasidi, A. S. and Abdelrahman, E. A., Pechini derived novel nanocomposites for efficient and reusable crystal violet dye remediation, *J. Ind. Chem. Soc.*, 103(1), 102373 (2026). https://doi.org/10.1016/j.jics.2025.102373

Dash, P. A., Mohanty, S. and Nayak, S. K., Synthesis and characterization of ZnO/MgO doped mesoporous bioactive glass: Enhanced bioactivity and antibacterial properties for bone tissue engineering applications, *Ceram. Int.*, 51(23), 38129–38140 (2025). https://doi.org/10.1016/j.ceramint.2025.06.049

Ebenezer, A. J. P., Caroline, A. L., Mayakannan, S., Dhivya, M., Sri, T. S. and Saravanan, V., Optimization of Green-synthesized Graphene Quantum Dots using Machine Learning for Neuroprotective Antioxidant Applications, *J. Environ. Nanotechnol.*, 15(2), 463–478 (2026). https://doi.org/10.13074/jent.2026.06.2622142

Elkady, F. M., Alsalamah, S. A., Hashem, A., saied, E., Abdelaziz, A. M., Tawab, A. A., Salama, A., Alsenani, F., Ibrahim, N. A., Basher, N. S., Abdulrahman, M. S. and Aufy, M., Synergistic antimicrobial and antibiofilm effects of mycosynthesized MnO–MgO bimetallic nanoparticles against drug-resistant pathogens, *BMC Microbio.*, 26(1), 488 (2026). https://doi.org/10.1186/s12866-026-05152-y

Fonye, N. G., Eya'ane, M. F., Ondoh, A. M., Kwati, L., Ndzeidze, G. N. and Paboudam, G. A., Biosynthesis, Characterization, and Potential Antimicrobial Studies of Silver–Magnesium Oxide Nanocomposites Mediated from Talinum fruticosum Leaf Extract, *J. Inorg. Organomet. Polym. Mater.*, 36(4), 2243–2265 (2026). https://doi.org/10.1007/s10904-025-04027-5

Gajendiran, J., Ramya, J. R., Vijayalakshmi, R., Balraju, P., Suresh, R., Thennarasu, G. and Gnanasekaran, L., Investigation on the structural, optical, and biofunctional properties of MgO-NiO nanocomposites under influence of calcined temperature, *Inorg. Chem. Commun.*, 181, 115163 (2025). https://doi.org/10.1016/j.inoche.2025.115163

Gamal, G. A., Ebnalwaled, A. A., Samir, M. and Said, A. H., Broccoli triggers the hemocompatibility of green nanoparticles, *Discover Nano*, 21(1), 214 (2026). https://doi.org/10.1186/s11671-026-04567-w

Ganesan, T., Muthukrishnan, S., Albeshr, M. F., Selvankumar, T., Pradeepkumar, S., Indumathi, K. P. and Anto, B., *Aerva lanata* flower extract mediated green synthesis of silver nanoparticles: Their characterization, in vitro antioxidants and antimicrobial investigations, *Polym. Adv. Technol.*, 35(3), e6354 (2024). https://doi.org/10.1002/pat.6354

Ganesan, T., Muthukrishnan, S., Anto, B., Mathaiyan, M., Kumar, S. P., Jayaprakash, R. and Suganya, M., RAPD Analysis, Synthesis of Zinc Oxide Nanoparticles Derived from *Aerva lanata* Flower: Characterization and Antimicrobial Screening, *Asian J. Chem.*, 35(9), 2153–2156 (2023). https://doi.org/10.14233/ajchem.2023.28066

Ganvir, H. V, Musrif, P. G., Satishkumar, P., Kadam, A. D., Saminathan, R. and Krishnaraj, C., Sustainable Synthesis of MgO Nanoparticles from Clerodendrum inerme Bast Fiber Extract: Physicochemical Characterization and Antibacterial Performance, *J. Environ. Nanotechnol.*, 15(2), 380–388 (2026a). https://doi.org/10.13074/jent.2026.06.2622227

Ganvir, V. Y., Satishkumar, P., Awachat, D. B., Rani, A., Talodhikar, V. and Krishnaraj, C., Biofabricated CuO Nanoparticle Reinforced Bamboo Fiber Coatings for Photocatalytic Antimicrobial and Superhydrophobic Biomedical Textile Applications, *J. Environ. Nanotechnol.*, 15(2), 330–343 (2026b). https://doi.org/10.13074/jent.2026.06.2622243

Ghasemzadeh, H., Nematollahzadeh, A., Vaseghi, Z. and Safajou-Jahankhanemlou, M., Synthesis, Characterization, and Assessment of Anticancer Activity of Green ZnO/MgO Bimetallic Nanoparticles against Breast Cancer Cells, *Part. Part. Syst. Characteriz.*, 42(8), e00016 (2025). https://doi.org/10.1002/ppsc.202500016

Imtiaz, H., Riaz, M. and Fatima, M., Design and characterization of CaO–MgO–SiO_2 materials for enhanced bioactivity in biomedical applications, *J. Mater. Res.,* 40(10), 1511–1522 (2025). https://doi.org/10.1557/s43578-025-01591-x

Jayamani, R., Krishnaveni, R., Sethupathi, M., Dixit, S., Devanesan, S., Shanmugaraj, K. and Palanisamy, G., Biosynthesis of Nickel Nanoparticles Using Aqueous *Aerva lanata* Extract and Their Utilization in Antimicrobial Activity, *Lumin.*, 40(11), e70364 (2025). https://doi.org/10.1002/bio.70364

Kattookaran, C. V., Govindasamy, R., Selvam, S. P. and Viswanathan, D., Biosynthesis of Ag doped MgO-Zno nanocomposite with Cassia alata plant leaves extract and assessment of their biological applications, *Next Mater.*, 8, 100820 (2025). https://doi.org/10.1016/j.nxmate.2025.100820

Krishnasamy, B., Gladston, A. K., Sekar, C. B. and Selvaraju, M., Investigation on the thermal, mechanical, and morphological characterization of peepal fiber-reinforced epoxy composites enhanced with micro-particulate *Ziziphus mauritiana* seed powder, *Revista Materia*, 31, e20250643 (2026). https://doi.org/10.1590/1517-7076-RMAT-2025-0643

Krishnasamy, B., Thirugapillai, P., Rajakannu, A. and Selvaraju, M., Optimization and multi-objective analysis of tensile, flexural and impact strength in nano-hybrid bio-composites reinforced with Helicteres isora, Holoptelea integrifolia fibers, and nanographene, *Revista Materia*, 30, e20240864 (2025). https://doi.org/10.1590/1517-7076-RMAT-2024-0864

Nagaraj, A., Ghosh, O. S. N., Ghneim, H. K., AlSheikh, Y. A., Mohammed, K., Poda, S. and Kalagatur, N. K., Fe_2O_3-type iron oxide nanoparticles from *Aerva lanata* leaf extract exhibit antibiofilm, discriminatory toxicity in cancer cells, and theranostic against oxidative stress in zebrafish, *Chem. Phy. Impact*, 10, 100849 (2025). https://doi.org/10.1016/j.chphi.2025.100849

Najm, M. A. A., Faraj, D. N., Najim, S. S., Jabir, M. S., Jawad, K. H., Ghotekar, S., Balasubramanian, B., Ismael, A. B. and Swelum, A., CuO@MgO Nanocomposite as a Promising Strategy for Multidrug-Resistant Bacteria: A Study the Mechanism of Action via In Silico Prediction, *BioNanoSci.*, 16(6), 422 (2026). https://doi.org/10.1007/s12668-026-02665-8

Obead, A. H. and Abbas, N. K., Green Synthesis of MgO Nanoparticles via Two Different Methods and Studying their Structural, Morphological, and Optical Properties, *Baghdad Sci. J.,* 22(8), 2638–2646 (2025). https://doi.org/10.21123/2411-7986.5027

Otabor, G. O. and Ikhuoria, E. U., Phytochemical-mediated Green Synthesis of Spherical Magnesium Oxide Nanoparticles Using Aqueous *Hevea brasiliensis* (Rubber Leaf) Extract for Biomedical (Antioxidant and Antibacterial) and Environmental (Photocatalytic Degradation of Methylene Blue Dye) Applications, *Chem. Afr.*, 9(5), 207 (2026). https://doi.org/10.1007/s42250-026-01707-8

Palithya, S., Gaddam, S. A., Kotakadi, V. S., Penchalaneni, J., Golla, N., Krishna, S. B. N. and Naidu, C. V., Green synthesis of silver nanoparticles using flower extracts of *Aerva lanata* and their biomedical applications, *Particulate Sci. Technol.*, 40(1), 84–96 (2022). https://doi.org/10.1080/02726351.2021.1919259

Periakaruppan, R., Chandrasekaran, N., Vijai Selvaraj, K. S., Thenmozhi, M. and Das, N. M., Synthesis, characterization, and antioxidant activity of Chrysanthemum indicum flower-mediated magnesium oxide nanoparticles, *Biomass Convers. Biorefine.*, 15(20), 27315–27320 (2025). https://doi.org/10.1007/s13399-024-05839-0

Radulescu, D. M., Neacsu, I. A., Vasile, B. S., Surdu, V. A., Oprea, O. C., Trusca, R. D., Chircov, C., Popescu, R. C., Ilie, C. I., Ditu, L. M., Drumea, V. and Andronescu, E., Green-Synthesized MgO Nanoparticles: Structural Insights and Antimicrobial Applications, *Int. J. Mol. Sci.*, 26(18), 9021 (2025). https://doi.org/10.3390/ijms26189021

Raguvaran, K., Kalpana, M., Devapriya, P., Kalaivani, S., Angelina, M., Krismastuti, F., Rasool, A. and Maheswaran, R., Eco-Friendly Synthesis of Silver Nanoparticles and Its Larvicidal Property Against Malaria, Filariasis, and Dengue Vectors, *Lumin.*, 40(7), e70266 (2025). https://doi.org/10.1002/bio.70266

Rana, G., Rao, S. K. and Chauhan, A., The efficient visible light assisted photocatalytic degradation of tetracycline and crystal violet using phyto-mediated magnesium oxide-zinc oxide nanocomposites, *J. Ind. Chem. Soc.*, 102(1), 101545 (2025). https://doi.org/10.1016/j.jics.2024.101545

Renuka, S., Hariharan, V., Arulraj, J. V., Sutharsan, P., Gokulakumar, B. and Dhanaraj, K., Evaluation of antibacterial activity using *Aerva lanata* and Millettia pinnata leaf extracts mediated ZnO and Cu-doped ZnO nanoparticles, *Global Nest J.,* 25(6), 48–54 (2023). https://doi.org/10.30955/gnj.004655

Sanjai, R., Rahul, A. M., Singh, P. K., Thirumavalavan, M., Velmurugan, D. and Pachaiappan, R., Analytical insights on identification and characterization of potential bioactive compounds from two renal lithiasis-resistant plants viz. *Aerva lanata* and *Aerva javanica, Microchem. J.*, 217, 114967 (2025). https://doi.org/10.1016/j.microc.2025.114967

Sanjana, R., Priyadharshini, S., Rajeshkumar and Anandan, J., Evaluation of Antimicrobial and Cytotoxic Effects of Eclipta prostrata-mediated Calcium Oxide Nanoparticle-incorporated Mouth Rinse, *J. Environ. Nanotechnol*., 14(1), 63–68 (2025). https://doi.org/10.13074/jent.2025.03.243941

Suresh, S., Thambidurai, S., Arumugam, J., Kandasamy, M., Pugazhenthiran, N., Balaji, D., Al-Asbahi, B. A., Reddy, N. R., Arunkumar, A. and Muneeswaran, T., Antibacterial activity and photocatalytic oxidative performance of zinc oxide nanorods biosynthesized using *Aerva lanata* leaf extract, *Inorg. Chem. Commun.*, 139, 109398 (2022). https://doi.org/10.1016/j.inoche.2022.109398

Thakur, S., Thakur, I. and Kumar, R., Doped MgO nanoparticles: enhanced photocatalytic degradation of organic dyes and antioxidant properties, *Mater. Sci. Eng. B*, 322, 118628 (2025). https://doi.org/10.1016/j.mseb.2025.118628

Vamsi, K. B. V, Durga, L. B., Tirupathi, R. P. and Ramachandra, R. K., Structural, optical, and antioxidant properties of biocompatible CuO-MgO nanocomposites, *Res. Mater.*, 26, 100695 (2025). https://doi.org/10.1016/j.rinma.2025.100695